The Astrophysical Journal Letters, 920:L42 (7pp), 2021 October 20 https://doi.org/10.3847/2041-8213/ac2cc1

Black Hole Mergers of AGN Origin in LIGO–Virgo's O1–O3a Observing Periods

V. Gayathri[1], Y. Yang[1], H. Tagawa[2], Z. Haiman[3], and I. Bartos[1]
[1] Department of Physics, University of Florida, PO Box 118440, Gainesville, FL 32611-8440, USA; imrebartos@ufl.edu
[2] Astronomical Institute, Graduate School of Science, Tohoku University, Aoba, Sendai 980-8578, Japan
[3] Department of Astronomy, Columbia University, 550 W. 120th Street, New York, NY 10027, USA
Received 2021 April 23; revised 2021 September 27; accepted 2021 October 2; published 2021 October 21

Abstract

The origin of the black hole mergers detected by LIGO–Virgo remains an open question. While the unusual mass and spin of a few events constrain their possible astrophysical formation mechanisms, it is difficult to classify the bulk of the observed mergers. Here we consider the distribution of masses and spins in LIGO–Virgo's first two observing catalogs. We show that, for black holes in the mass gap, our fiducial active galactic nucleus (AGN) model is preferred over a parametric mass–spin model fit to the full GWTC-2 merger sample (Bayes factor $\mathcal{B} > 10$). This preference, nevertheless, depends on uncertain AGN model parameters. We further show that a 20% fractional contribution of the detected events of an AGN-disk origin reproduces well the observed black hole mass distribution in the pair-instability mass gap, while only marginally contributing to the lower-mass detected population. The overall AGN contribution corresponds to a black hole merger rate of about 2.5 $\mathrm{Gpc}^{-3}\,\mathrm{yr}^{-1}$, comparable to theoretical expectations.

Unified Astronomy Thesaurus concepts: Gravitational wave astronomy (675); Gravitational waves (678)

Supporting material: machine-readable table

1. Introduction

Stellar-mass binary black holes (BHs) can be the end results of several distinct astrophysical processes. They can form from isolated stellar binaries (Portegies Zwart & Yungelson 1998; Belczynski et al. 2002; Marchant et al. 2016; de Mink & Mandel 2016) or triples (Antonini et al. 2014; Kimpson et al. 2016; Veske et al. 2020), dynamical interactions in star clusters (Sigurdsson & Hernquist 1993; Portegies Zwart & McMillan 2000), primordial BHs formed in the early universe (Carr & Hawking 1974), and in the accretion disks of active galactic nuclei (AGNs; McKernan et al. 2012; Bartos et al. 2017b; Stone et al. 2017; Tagawa et al. 2020b).

The origin of BH mergers discovered by the LIGO (Aasi et al. 2015) and Virgo (Acernese et al. 2015) gravitational-wave observatories is not yet known (Abbott et al. 2019, 2021a). Nonetheless, some initial clues have emerged that challenge the isolated stellar binary origin of at least some of the events. These clues include the detection of at least one BH in the pair-instability mass gap ($50\,M_\odot \lesssim M \lesssim 120\,M_\odot$; Woosley & Heger 2015) that may not be populated through isolated stellar evolution (Abbott et al. 2020; although supernova theory remains uncertain; Belczynski et al. 2020; Di Carlo et al. 2020; Farmer et al. 2020) and mergers with large BH spins that are misaligned from the binary orbital axis (Abbott et al. 2021b).

In this Letter we examine which of the observed mergers may have occurred in AGNs, and use this to estimate the AGN fractional contribution to LIGO–Virgo's events. We carried out a Bayesian model comparison in which we contrasted the likelihood of each merger originating in an AGN disk to the likelihood of origin from the empirical mass–spin distribution obtained from the full observed BH population. Additionally, we considered the maximum AGN contribution to the total merger rate that is still consistent with the observed BH mass distribution.

A major advantage of such a comparison is that it avoids relying on the uncertain parameters and fractional contributions of other astrophysical scenarios. There are also several disadvantages: (i) our analysis relies on a parametric model fit on the observed data (Abbott et al. 2021b), which is not guaranteed to closely resemble the true underlying distribution; (ii) the adopted parametric model was fit to all detected events, while we carried out model comparison for individual events, potentially introducing a bias; (iii) the parametric model was fit on the full data set that also includes AGN-assisted mergers, although this should make the fit more favorable to AGN-related events and make the model comparison more conservative. In addition, the model parameters of AGN-assisted mergers are themselves uncertain. To characterize this uncertainty we considered two AGN scenarios with astrophysically motivated sets of parameters.

While the ultimate answer to which events correspond to different formation channels may come once we gain a detailed understanding of the relevant formation scenarios, the analysis presented here provides a first indication of the contribution of AGNs to the overall detection rate by LIGO–Virgo.

2. Model Comparison

We carried out model comparisons for individual gravitational-wave events. For merger population model A, we computed the probability distribution $P_{\mathrm{pop}}(\vec{\theta}|A)$ of binary parameters $\vec{\theta}$. For our AGN model this was done by simulating a large number of mergers and taking the obtained parameter distribution, while for our LIGO–Virgo model we adopted this distribution from Abbott et al. (2021a) that was obtained by fitting a model on the observed data. Within $\vec{\theta}$ we considered the binary's chirp mass $\mathcal{M} = (m_1 m_2)^{3/5}(m_1 + m_2)^{-1/5}$; mass ratio $q = m_2/m_1$; effective spin $\chi_{\mathrm{eff}} = cG^{-1}(m_1 + m_2)^{-1}(\boldsymbol{S}_1/m_1 + \boldsymbol{S}_2/m_2)\boldsymbol{L}/|\boldsymbol{L}|$, which describes the objects' spin component parallel to the binary's orbital axis; and precessing spin $\chi_{\mathrm{p}} =$

$\max\left(\boldsymbol{S}_1/m_1, \frac{2+3q/2}{q^2}\boldsymbol{S}_2/m_2\right) \times \boldsymbol{L}/|\boldsymbol{L}|$, which describes the projection of component spin vectors perpendicular to the orbital axis (Hannam et al. 2014). Here, m_1 and m_2 are the masses in the binary with $m_1 > m_2$, $\boldsymbol{S}_1$ and $\boldsymbol{S}_1$ are the two objects' spin vectors, and $\boldsymbol{L}$ is the binary's orbital angular momentum vector.

The posterior probability of model A given gravitational-wave data $\boldsymbol{x}$ from a single event is (Mandel et al. 2019; Vitale et al. 2020; Gayathri et al. 2020)

$$P(A|\boldsymbol{x}) = \pi(A)\frac{\int d\vec{\theta} P(\vec{\theta}|\boldsymbol{x})\pi(\vec{\theta})^{-1}P_{\rm pop}(\vec{\theta}|A)}{\int d\vec{\theta} P_{\rm det}(\vec{\theta})P_{\rm pop}(\vec{\theta}|A)}. \quad (1)$$

Here, $\pi(A)$ is the prior probability of A. $P(\vec{\theta}|\boldsymbol{x})$ is the probability density of true event parameters $\vec{\theta}$ for the gravitational wave. It is obtained using parameter estimation algorithms based on the observed data. We adopted $P(\vec{\theta}|\boldsymbol{x})$ for observed events from Abbott et al. (2021a) and Abbott et al. (2019). For these we divided the posterior by the prior probability provided by these analyses. $P_{\rm det}(\vec{\theta})$ is the detection probability for an event with true parameters $\vec{\theta}$, which we obtained by computing the cosmic volume within which the gravitational wave with these parameters would give a signal-to-noise ratio of >8 combined for two LIGO detectors, We adopted a typical LIGO noise curve during O3, while for O1 and O2 we adopted a relative decrease of sensitivity of 50% and 25%, respectively, compared to O3. The prior probability density $\pi(\vec{\theta})$ assumes uniform source distribution in comoving volume and source-frame time. The integral in Equation (1) is approximated by summing the Monte Carlo samples of the underlying distributions obtained by LIGO–Virgo. We marginalized over binary parameters not considered here in $\vec{\theta}$. We computed the Bayes factor for population models A and B as

$$\mathcal{B}_{\rm B,A} = \frac{P(\boldsymbol{x}|B)}{P(\boldsymbol{x}|A)} = \frac{P(B|\boldsymbol{x})}{P(A|\boldsymbol{x})}\frac{\pi(B)}{\pi(A)}. \quad (2)$$

3. Model 1: Binary Mergers in AGNs

Following Bartos et al. (2017b), we adopted a geometrically thin, optically thick, radiatively efficient, steady-state accretion disk expected in AGNs. We used a viscosity parameter $\alpha = 0.1$, radiative efficiency $\epsilon = 0.1$, fiducial supermassive BH mass $M_\bullet = 10^6\,M_\odot$, and accretion rate $0.1\dot{M}_{\rm Edd}$, where $\dot{M}_{\rm Edd}$ is the Eddington accretion rate. We computed the expected mass and spin distributions of binary mergers in AGNs following Yang et al. (2020) and Tagawa et al. (2020b, 2020a). For simplicity, we adopted a Salpeter initial mass function $dN/dm \propto m^{-2.35}$ for BHs and a normal initial mass function $m/M_\odot \sim N(1.49, 0.19)$ for neutron stars (NSs; Özel & Freire 2016). We assumed that the total mass of the BH population is 1.6% of the stellar mass in galactic centers and the number of NSs is 10 times that of BHs. We also took into account the mass segregation in the spatial distributions of BHs and NSs following O'Leary et al. (2009) and Gondán et al. (2018).

BHs and NSs (hereafter compact objects) orbiting the central supermassive BH will periodically cross the AGN disk. We simulated the process of orbital alignment with the disk following Yang et al. (2019). Compact objects were assumed to migrate from their original locations inward once they have been aligned with the AGN disk. We adopted the type I and type II migration rates given in Tagawa et al. (2020a). Compact objects can undergo close encounters with other objects around the supermassive BH. When this happens in the AGN disk, the surrounding gas might remove enough energy such that the two objects involved in the close encounter are able to form a binary (Goldreich et al. 2002; Tagawa et al. 2020b). We found through numerical simulations that the flux of compact objects passing by an object in the AGN disk can be approximated as $\phi_i = 4\times10^{-8}\,{\rm au}^{-2}{\rm yr}^{-1}(\rho_i/10^4\,{\rm pc}^{-3})$, where the index i can refer to BHs or NSs, and ρ_i is their number density in the galactic center. The orientation of their velocity was assumed to be isotropically distributed, following a normal distribution $N(0, \sigma_{\rm v}^2)$ in each spatial dimension, where $\sigma_{\rm v}^2 = 2.5\times10^3(r/{\rm pc})^{-1}({\rm km/s})^2$. The rate for close encounters in the AGN disk is then $\Gamma_{\rm en,i} \simeq \sqrt{3}\,\phi_i r_{\rm H}^2\langle v_{\rm rel}\rangle/\sigma_{\rm v} \sim \sqrt{3}\,\phi_i r_{\rm H}^2\sqrt{1+v_{\rm kep}^2/\sigma_{\rm v}^2}$, where $r_{\rm H}$ is the mutual Hill radius and $v_{\rm kep}$ is the Keplerian velocity of an orbit with radius r. When the two objects have small relative velocity, the gaseous friction is able to remove the necessary energy for binary formation (Tagawa et al. 2020b). With these assumptions gas capture typically occurs in the inner regions (10^{-4}–10^{-2} pc) of the AGN where gas density is high.

We assumed that binaries can also form via three-body interactions (Binney & Tremaine 2008), with an estimated formation rate of $\Gamma_{\rm 3bbf,i} \simeq \frac{1}{2}n_{\rm i}^2 b_{\rm str}^5 v_{\rm rel}$, where n_i is the density of BHs or NSs and $b_{\rm str} = \min\{b_{90}, r_{\rm H}\}$, $b_{90} = Gm_{\rm tot}/v_{\rm rel}^2$.

BHs capture gas from the AGN disk while they are moving in or crossing the disk, changing their masses and spins. The spin magnitude after $\Delta m_{\rm BH}$ accreted mass is (Bardeen 1970; Tagawa et al. 2020a)

$$a^{\rm f} = \frac{1}{3}\frac{r_{\rm isco}^2}{f_{\rm acc}}\left[4 - \left(3\frac{r_{\rm isco}}{f_{\rm acc}^2} - 1\right)^{1/2}\right], \quad (3)$$

where $f_{\rm acc} = (m_{\rm BH} + \Delta m_{\rm BH})/m_{\rm BH}$ and $r_{\rm isco}$ is the radius of the innermost stable circular orbit (ISCO) in gravitational units. The BHs may possess minidisks. If the spin angular momentum $\boldsymbol{J}_{\rm BH} = \vec{a}\sqrt{Gm_{\rm BH}^3 R_{\rm g}}$ of a BH is misaligned with its inner minidisk, they will tend to align due to Lense–Thirring precession. The inner parts of the minidisk is defined by a so-called warp radius $R_{\rm warp}$ that is given by (Volonteri et al. 2007)

$$R_{\rm warp}/R_{\rm g} = 3.6\times10^2|\vec{a}|^{5/8}m_{\rm BH}^{1/8}\lambda^{-1/4}\left(\frac{\nu_2}{\nu_1}\right)\alpha^{-1/2}. \quad (4)$$

Here, λ is the Eddington ratio, ν_1 is the viscosity corresponding to angular momentum transfer in the accretion disk, and ν_2 is the viscosity responsible for warp propagation. We assumed $\nu_2/\nu_1 = 50$. We also assumed that the spin of a BH can align with the total angular momentum $\boldsymbol{J}_{\rm tot} = \boldsymbol{J}_{\rm BH} + \boldsymbol{J}_{\rm warp}$ in each time step of our simulations, where $J_{\rm warp} \simeq \Delta m_{\rm BH}\sqrt{Gm_{\rm BH}R_{\rm warp}}$. Following Tagawa et al. (2020a), we assumed that the direction of $\boldsymbol{J}_{\rm warp}$ is aligned with AGN-disk angular momentum for a single BH and is aligned with the orbital angular momentum for a BH in binary.

The direction of orbital angular momentum of binaries evolves due to accretion torques. We assumed that the orbital angular momentum after $\Delta m_{\rm Bin}$ being captured by the binary is

$\vec{J}^{\rm f}_{\rm bin} = \boldsymbol{J}_{\rm bin} + \boldsymbol{J}_{\rm gas}$ (Tagawa et al. 2020a; Lubow et al. 1999) with $\boldsymbol{J}_{\rm gas} \simeq \Delta m_{\rm Bin}\sqrt{G m_{\rm bin} s}\,\hat{J}_{\rm AGN}$, where s is the separation of the binary and $\hat{J}_{\rm AGN}$ is the direction of AGN-disk angular momentum.

When a binary travels in the AGN disk, the surrounding gas can provide a drag force on the binary, which will reduce its separation. We followed the results of Kim & Kim (2007) and Kim et al. (2008) for dynamical force in gaseous medium and assumed that the drag force is $F_{\rm df}\mathcal{M}^2 = const.$ when $\mathcal{M} > 8$, where $\mathcal{M}$ is the Mach number. Recent simulations of binary evolution give similar results within a factor of 2 (Antoni et al. 2019; Kaaz et al. 2021), although Li et al. (2021) find no gas-driven contraction for some orbital parameters.

When the orbital separation of a binary is sufficiently compact, gravitational radiation dominates the dynamical drag force. We assumed that the hardening rate is the combination of the contribution from dynamical friction and GW radiation.

The spatial distribution in galactic nuclei is not yet well constrained. While we assumed above an isotropic initial distribution, vector resonant relaxation could substantially reduce the BHs' initial velocity dispersion (Szölgyén & Kocsis 2018), which can increase the chance of capture during a close encounter as well as the probability of forming binaries via three-body encounters. To characterize this scenario, we additionally considered below the AGN-assisted merger model of Tagawa et al. (2021a) that adopts a small initial velocity dispersion of $\sim 0.2 v_{\rm kep}$. Beyond the difference in the velocity dispersion, Tagawa et al. (2021a) also adopt a BH initial mass function with a maximum mass of $15\,M_\odot$ (see $50\,M_\odot$ for the fiducial model), reflecting the high metallicity observed near AGN disks.

4. Model 2: LIGO–Virgo GWTC-2

To differentiate AGN-assisted mergers from the rest of LIGO–Virgo's detections, we considered the population properties of the 47 binary mergers identified by LIGO–Virgo for the available observing runs O1, O2, and O3a (Abbott et al. 2019, 2021a). We adopted the obtained parameter distributions for the "Power Law + Peak mass" model of Abbott et al. (2021b) (hereafter GWTC-2 model). For m_1 this model gives

$$\begin{aligned}&\pi(m_1|\lambda_{\rm peak}, \alpha, m_{\rm min}, \delta_m, m_{\rm max}, \mu_m, \sigma_m)\\ &= (1-\lambda_{\rm peak})\mathfrak{P}(m_1|-\alpha, m_{\rm max})S(m_1|m_{\rm min}, \delta_m)\\ &\quad + \lambda_{\rm peak}G(m_1|\mu_m, \sigma_m)S(m_1|m_{\rm min}, \delta_m).\end{aligned} \tag{5}$$

Here, the three functions on the right-hand side describe a normalized power-law distribution with spectral index $-\alpha$ and high-mass cutoff $m_{\rm max}$ ($\mathfrak{P}$), a normalized Gaussian distribution with mean μ_m and width σ_m (G), and a smoothing function that rises from 0 to 1 between $m_{\rm min}$ and $m_{\rm min} + \delta_m$ (S). The parameter $\lambda_{\rm peak}$ is a mixing fraction determining the relative prevalence of mergers in power-law and Gaussian distribution.

We adopted the conditional mass ratio distribution

$$\pi(q|\beta_q, m_1, m_{\rm min}, \delta_m) \propto q^{\beta_q}S(qm_1|m_{\rm min}, \delta_m). \tag{6}$$

The mass distribution model is represented by eight parameters, namely, λ_{peak}, α, $m_{\rm min}$, δ_m, $m_{\rm max}$, μ_m, σ_m, and β_q. Here, m_1 and m_2 samples were extracted from the hyperparameter space model, and these parameter estimations are reported by Abbott et al. (2021b, see their Figure 16), and $S(qm_1|m_{\rm min}, \delta_m)$ is a smoothing function (see Equation B6 of Abbott et al. 2021b).

Similarly, we considered their default spin model for spin estimation. This dimensionless spin magnitude model is represented by two parameters, namely, α_χ and β_χ by a beta distribution, $\pi(\chi_{1,2}|\alpha_\chi, \beta_\chi) = {\rm Beta}(\alpha_x, \beta_x)$. These parameters are known as standard shape parameters that determine the distribution's mean and variance. Here we assume the same distribution for χ_1 and χ_2. The cosine of the tilt angle between component spin and binary orbital angular momentum is represented by two parameters, namely, ζ and σ_t. This cosine angle is distributed as a mixture of two populations: ($\mathcal{J}$ isotropic distribution + G_t truncated Gaussian) and $\pi(\cos\theta_{1,2}|\zeta, \sigma_t) = \zeta G_t(\cos\theta_{1,2}|\sigma_t) + (1-\zeta)\mathcal{J}(\cos\theta_{1,2})$.

5. Results

We computed the Bayes factor for each binary merger detected by LIGO–Virgo in their O1, O2, and O3a observing runs by comparing our fiducial AGN model to the baseline GWTC-2 model. We determined the Bayes factor using the parameters $\mathcal{M}$, $\chi_{\rm eff}$, $\chi_{\rm p}$, and q. We also determined the Bayes factor using pairs of parameters involving the chirp mass $\mathcal{M}$ and either $\chi_{\rm eff}$, $\chi_{\rm p}$, or q.

In Table 1 we present a detailed list of Bayes factors for each event. We see that, for our fiducial AGN model, 10 out of the 48 gravitational-wave events have Bayes factor $\mathcal{B} > 10$, which we use here as a threshold to indicate probable AGN origin (Kass & Raftery 1995).

To show the parameters of the binaries that are distinct from the GWTC-2 model and are likely of AGN origin, in Figure 1 we show 2D slices of the parameter distributions. These slices include the $\mathcal{M} - \chi_{\rm eff}$, $\mathcal{M} - \chi_{\rm p}$, and $\mathcal{M} - q$ combinations. The numerical values of the Bayes factors for the above three combinations are listed in Table 1. We see that our fiducial AGN model is favored mainly for high-mass, high-spin sources, where the GWTC-2 model has weaker support. Note that the AGN model of Tagawa et al. (2021a) generally favors lower masses as its BH initial mass function extends only up to $15\,M_\odot$, and accordingly high-mass binaries have less support for this model.

We estimated the overall fraction of AGN-assisted mergers within LIGO–Virgo's detections. We considered a chirp mass threshold of $\mathcal{M}_{\rm th} = 40\ M_\odot$ above which all (four out of four) events are favored to have an AGN origin with $\mathcal{B} > 10$. We then computed the overall AGN-assisted merger rate that corresponds to four expected detections above this mass from AGNs by LIGO–Virgo during O1, O2, and O3a. In this computation we adjusted the overall AGN merger rate density in comoving volume. We assumed a uniform rate density distribution, reflecting the shallow cosmic evolution of the merger rate (Yang et al. 2020). All other model parameters were adopted as described above in our fiducial model, and were not adjusted in this fit. The expected number of detections was calculated using LIGO's typical O3 noise curve for the three observing runs, the observing times, and the binary gravitational waveforms (NRSur7qd4 waveform model) as functions of binary mass and spin. We required a network-wide signal-to-noise (LIGO-Handford and LIGO-Livingston detectors) ratio of 8 (individual detector signal-to-noise ratio greater than 4) for detection. With this we estimated the AGN BH merger rate to be about $2.5\,{\rm Gpc}^{-3}\,{\rm yr}^{-1}$. This corresponds to an overall expected $\sim$15 binary mergers of AGN origin in LIGO–

Table 1
GWTC-2 Gravitational-wave Event Parameters and Bayes Factors

Event	Estimated Source Parameters						Bayes Factor				
	m_1	m_2	$\mathcal{M}$	q	$\chi_{\rm eff}$	$\chi_{\rm p}$	$\mathcal{M}\chi_{\rm eff}$	$\mathcal{M}\chi_p$	$\mathcal{M}q$	$\mathcal{M}$-χ_{eff}-χ_p-q	
GW190408_181802	$24.6^{+3.42}_{-5.08}$	$18.44^{+3.6}_{-3.27}$	$18.34^{+1.21}_{-1.88}$	$0.75^{+0.24}_{-0.21}$	$-0.03^{+0.2}_{-0.13}$	$0.39^{+0.31}_{-0.37}$	0.88	1.66	0.42	5.46	0.19
GW190412	$30.04^{+5.12}_{-4.62}$	$8.33^{+0.92}_{-1.62}$	$13.26^{+0.33}_{-0.42}$	$0.28^{+0.06}_{-0.12}$	$0.25^{+0.11}_{-0.08}$	$0.3^{+0.16}_{-0.19}$	1.29	0.94	1.6	$<10^{-2}$	$<10^{-2}$
GW190413_052954	$34.58^{+7.95}_{-12.41}$	$23.64^{+6.69}_{-7.44}$	$24.63^{+4.08}_{-5.57}$	$0.69^{+0.29}_{-0.27}$	$-0.01^{+0.34}_{-0.28}$	$0.41^{+0.31}_{-0.42}$	3.61	3.25	0.91	$<10^{-2}$	$<10^{-2}$
GW190413_134308	$47.5^{+10.42}_{-13.25}$	$31.81^{+10.81}_{-11.65}$	$32.94^{+5.32}_{-8.28}$	$0.69^{+0.31}_{-0.28}$	$-0.04^{+0.28}_{-0.24}$	$0.56^{+0.41}_{-0.37}$	6.65	15	4.72	$<10^{-2}$	$<10^{-2}$
GW190421_213856	$41.43^{+6.82}_{-10.46}$	$31.91^{+8.85}_{-8.02}$	$31.2^{+4.25}_{-5.93}$	$0.79^{+0.3}_{-0.19}$	$-0.06^{+0.27}_{-0.23}$	$0.48^{+0.36}_{-0.4}$	7.27	10.0	1.86	$<10^{-2}$	$<10^{-2}$
GW190424_180648	$40.41^{+7.18}_{-11.03}$	$31.84^{+7.71}_{-7.56}$	$31.06^{+4.57}_{-5.79}$	$0.81^{+0.29}_{-0.17}$	$0.13^{+0.23}_{-0.22}$	$0.52^{+0.38}_{-0.38}$	3.81	12	1.38	32	6.67
GW190503_185404	$43.26^{+8.0}_{-9.17}$	$28.45^{+7.91}_{-7.71}$	$30.17^{+4.25}_{-4.22}$	$0.65^{+0.23}_{-0.29}$	$-0.03^{+0.26}_{-0.19}$	$0.38^{+0.29}_{-0.42}$	0.6	5.2	2.65	44	11
GW190512_180714	$23.23^{+5.68}_{-5.35}$	$12.58^{+2.52}_{-3.54}$	$14.62^{+1.03}_{-1.28}$	$0.54^{+0.18}_{-0.37}$	$0.03^{+0.13}_{-0.12}$	$0.22^{+0.17}_{-0.37}$	1.04	0.7	0.44	28	8.74
GW190513_205428	$35.65^{+9.1}_{-9.54}$	$18.0^{+4.14}_{-7.64}$	$21.57^{+1.88}_{-3.77}$	$0.5^{+0.18}_{-0.42}$	$0.11^{+0.17}_{-0.28}$	$0.31^{+0.23}_{-0.39}$	13	1.3	1.33	119	74
GW190514_065416	$39.08^{+8.4}_{-15.08}$	$28.57^{+8.47}_{-9.01}$	$28.73^{+5.0}_{-7.56}$	$0.75^{+0.32}_{-0.22}$	$-0.19^{+0.31}_{-0.29}$	$0.46^{+0.33}_{-0.39}$	39	6.53	1.4	$<10^{-2}$	$<10^{-2}$
GW190517_055101	$37.43^{+7.61}_{-11.74}$	$25.33^{+7.28}_{-6.88}$	$26.61^{+3.99}_{-4.0}$	$0.68^{+0.29}_{-0.27}$	$0.52^{+0.19}_{-0.19}$	$0.49^{+0.29}_{-0.3}$	42	7.34	1.39	$<10^{-2}$	$<10^{-2}$
GW190519_153544	$66.11^{+12.33}_{-10.69}$	$40.6^{+11.03}_{-11.0}$	$44.56^{+7.23}_{-6.34}$	$0.61^{+0.19}_{-0.28}$	$0.31^{+0.22}_{-0.2}$	$0.44^{+0.29}_{-0.35}$	3.18	34	40	68	44
GW190521_074359	$42.23^{+4.85}_{-5.95}$	$32.87^{+6.32}_{-5.45}$	$32.06^{+2.45}_{-3.22}$	$0.78^{+0.21}_{-0.19}$	$0.09^{+0.13}_{-0.1}$	$0.4^{+0.29}_{-0.32}$	156	8.17	2.34	$<10^{-2}$	$<10^{-2}$
GW190521	$94.73^{+18.45}_{-28.79}$	$69.43^{+23.99}_{-22.24}$	$69.24^{+10.55}_{-16.79}$	$0.75^{+0.35}_{-0.22}$	$0.03^{+0.4}_{-0.31}$	$0.67^{+0.44}_{-0.26}$	1.71	341	101	1979	259
GW190527_092055	$36.69^{+9.25}_{-16.03}$	$22.53^{+8.13}_{-10.64}$	$24.3^{+4.26}_{-9.46}$	$0.63^{+0.32}_{-0.32}$	$0.11^{+0.28}_{-0.28}$	$0.44^{+0.35}_{-0.44}$	22	2.9	1.16	$<10^{-2}$	$<10^{-2}$
GW190602_175927	$69.05^{+13.07}_{-15.86}$	$48.24^{+18.01}_{-13.59}$	$49.2^{+8.72}_{-8.8}$	$0.71^{+0.33}_{-0.25}$	$0.07^{+0.24}_{-0.26}$	$0.42^{+0.31}_{-0.41}$	17	37	31	189	72
GW190620_030421	$57.16^{+12.53}_{-15.72}$	$35.35^{+11.97}_{-12.35}$	$38.19^{+6.39}_{-8.32}$	$0.62^{+0.27}_{-0.32}$	$0.33^{+0.25}_{-0.22}$	$0.43^{+0.28}_{-0.36}$	1.17	16	15	134	39
GW190630_185205	$35.02^{+5.63}_{-6.88}$	$23.78^{+5.13}_{-5.12}$	$24.94^{+2.1}_{-2.03}$	$0.68^{+0.22}_{-0.27}$	$0.09^{+0.13}_{-0.12}$	$0.32^{+0.23}_{-0.31}$	29	2.28	0.9	$<10^{-2}$	$<10^{-2}$
GW190701_203306	$54.08^{+8.01}_{-11.87}$	$40.77^{+12.16}_{-8.59}$	$40.26^{+4.92}_{-5.49}$	$0.76^{+0.31}_{-0.21}$	$-0.07^{+0.29}_{-0.23}$	$0.42^{+0.31}_{-0.42}$	22	27	12	83	15
GW190706_222641	$66.84^{+15.59}_{-14.51}$	$38.33^{+13.64}_{-14.44}$	$42.82^{+7.18}_{-9.79}$	$0.58^{+0.25}_{-0.34}$	$0.28^{+0.28}_{-0.26}$	$0.38^{+0.28}_{-0.39}$	0.3	18	41	$<10^{-2}$	$<10^{-2}$
GW190707_093326	$11.58^{+1.71}_{-3.32}$	$8.38^{+1.65}_{-1.42}$	$8.55^{+0.46}_{-0.56}$	$0.73^{+0.27}_{-0.24}$	$-0.05^{+0.08}_{-0.1}$	$0.29^{+0.23}_{-0.39}$	0.52	0.42	0.06	$<10^{-2}$	$<10^{-2}$
GW190708_232457	$17.53^{+2.26}_{-4.76}$	$13.21^{+2.75}_{-2.02}$	$13.16^{+0.65}_{-0.9}$	$0.76^{+0.28}_{-0.21}$	$0.02^{+0.08}_{-0.1}$	$0.29^{+0.23}_{-0.43}$	2.16	1.03	0.32	$<10^{-2}$	$<10^{-2}$
GW190719_215514	$36.59^{+10.47}_{-18.24}$	$20.64^{+6.93}_{-9.17}$	$23.39^{+3.97}_{-6.74}$	$0.57^{+0.29}_{-0.37}$	$0.31^{+0.31}_{-0.28}$	$0.44^{+0.3}_{-0.36}$	0.34	2.68	1.15	382	284
GW190720_000836	$13.38^{+3.04}_{-6.56}$	$7.82^{+2.19}_{-2.25}$	$8.94^{+0.81}_{-0.51}$	$0.58^{+0.3}_{-0.36}$	$0.18^{+0.12}_{-0.14}$	$0.33^{+0.22}_{-0.43}$	3.17	0.52	0.09	$<10^{-2}$	$<10^{-2}$
GW190727_060333	$38.04^{+6.1}_{-9.63}$	$29.44^{+8.39}_{-7.07}$	$28.67^{+3.67}_{-5.39}$	$0.8^{+0.32}_{-0.18}$	$0.11^{+0.25}_{-0.26}$	$0.47^{+0.36}_{-0.41}$	0.25	7.68	1.31	29	64
GW190728_064510	$12.29^{+2.22}_{-7.11}$	$8.09^{+2.55}_{-1.7}$	$8.62^{+0.33}_{-0.54}$	$0.66^{+0.37}_{-0.3}$	$0.12^{+0.07}_{-0.19}$	$0.29^{+0.2}_{-0.37}$	3.4	0.38	0.07	$<10^{-2}$	$<10^{-2}$
GW190731_140936	$41.54^{+9.11}_{-11.92}$	$28.82^{+9.34}_{-9.77}$	$29.6^{+5.21}_{-7.1}$	$0.71^{+0.3}_{-0.25}$	$0.06^{+0.24}_{-0.24}$	$0.4^{+0.3}_{-0.45}$	3.86	4.93	2.1	85	33
GW190803_022701	$37.34^{+7.15}_{-10.48}$	$27.19^{+8.22}_{-7.89}$	$27.27^{+4.03}_{-5.77}$	$0.75^{+0.31}_{-0.22}$	$-0.03^{+0.26}_{-0.25}$	$0.44^{+0.33}_{-0.42}$	3.86	5.1	1.26	95	27
GW190814	$23.21^{+1.0}_{-1.12}$	$2.59^{+0.09}_{-0.08}$	$6.09^{+0.06}_{-0.06}$	$0.11^{+0.01}_{-0.01}$	$-0.0^{+0.06}_{-0.06}$	$0.04^{+0.03}_{-0.04}$	0.02	0.05	49	$<10^{-2}$	$<10^{-2}$
GW190828_063405	$32.13^{+4.05}_{-5.72}$	$26.18^{+4.79}_{-4.62}$	$24.96^{+2.14}_{-3.46}$	$0.82^{+0.22}_{-0.15}$	$0.19^{+0.16}_{-0.15}$	$0.43^{+0.3}_{-0.36}$	0.66	2.35	0.53	5.64	11.3
GW190828_065509	$24.04^{+7.06}_{-7.16}$	$10.25^{+2.18}_{-3.61}$	$13.35^{+0.95}_{-1.2}$	$0.43^{+0.16}_{-0.38}$	$0.08^{+0.16}_{-0.16}$	$0.3^{+0.23}_{-0.38}$	3.05	1.2	0.59	$<10^{-2}$	$<10^{-2}$
GW190909_114149	$45.94^{+13.21}_{-53.03}$	$28.16^{+12.53}_{-14.0}$	$30.63^{+7.25}_{-17.44}$	$0.61^{+0.38}_{-0.34}$	$-0.06^{+0.35}_{-0.41}$	$0.52^{+0.38}_{-0.39}$	3.64	4.57	2.36	$<10^{-2}$	$<10^{-2}$
GW190910_112807	$43.94^{+6.3}_{-7.56}$	$35.52^{+7.1}_{-6.31}$	$34.27^{+4.09}_{-4.13}$	$0.82^{+0.23}_{-0.15}$	$0.02^{+0.18}_{-0.18}$	$0.4^{+0.32}_{-0.39}$	6.41	9.71	2.93	8.56	0.0
GW190915_235702	$35.26^{+6.34}_{-9.63}$	$24.41^{+6.23}_{-5.67}$	$25.26^{+2.66}_{-3.2}$	$0.69^{+0.27}_{-0.27}$	$0.02^{+0.25}_{-0.2}$	$0.55^{+0.39}_{-0.36}$	1.95	5.82	0.96	$<10^{-2}$	$<10^{-2}$
GW190924_021846	$8.85^{+2.0}_{-6.96}$	$5.03^{+1.88}_{-1.35}$	$5.76^{+0.21}_{-0.24}$	$0.57^{+0.37}_{-0.36}$	$0.03^{+0.09}_{-0.3}$	$0.24^{+0.18}_{-0.4}$	0.08	0.11	0.03	$<10^{-2}$	$<10^{-2}$
GW190929_012149	$81.24^{+33.4}_{-32.65}$	$24.03^{+10.66}_{-19.4}$	$35.84^{+8.24}_{-14.72}$	$0.3^{+0.16}_{-0.53}$	$0.01^{+0.32}_{-0.34}$	$0.58^{+0.44}_{-0.32}$	8.11	8.95	173	$<10^{-2}$	$<10^{-2}$

Table 1
(Continued)

Event	Estimated Source Parameters						Bayes Factor				
	m_1	m_2	$\mathcal{M}$	q	$\chi_{\rm eff}$	$\chi_{\rm p}$	$\mathcal{M}\chi_{\rm eff}$	$\mathcal{M}\chi_p$	$\mathcal{M}q$	$\mathcal{M}$-χ_{eff}-χ_p-q	
GW190930_133541	$12.3^{+2.34}_{-12.4}$	$7.83^{+3.32}_{-1.71}$	$8.51^{+0.46}_{-0.49}$	$0.64^{+0.45}_{-0.3}$	$0.14^{+0.15}_{-0.31}$	$0.34^{+0.24}_{-0.4}$	0.26	11	4721	$<10^{-2}$	$<10^{-2}$
GW150914	$35.65^{+3.1}_{-4.66}$	$30.6^{+4.39}_{-3.02}$	$28.6^{+1.46}_{-1.66}$	$0.86^{+0.2}_{-0.12}$	$-0.01^{+0.13}_{-0.12}$	$0.34^{+0.25}_{-0.45}$	0.26	0.44	0.1	$<10^{-2}$	$<10^{-2}$
GW151012	$23.21^{+5.46}_{-14.94}$	$13.62^{+4.79}_{-4.07}$	$15.22^{+1.19}_{-2.08}$	$0.59^{+0.35}_{-0.36}$	$0.05^{+0.2}_{-0.31}$	$0.33^{+0.25}_{-0.45}$	1.83	1.24	0.5	$<10^{-2}$	$<10^{-2}$
GW151226	$13.72^{+3.23}_{-8.77}$	$7.68^{+2.55}_{-2.19}$	$8.86^{+0.28}_{-0.33}$	$0.56^{+0.33}_{-0.38}$	$0.18^{+0.12}_{-0.2}$	$0.49^{+0.32}_{-0.39}$	1.82	1.89	0.8	$<10^{-2}$	$<10^{-2}$
GW170104	$30.84^{+5.58}_{-7.33}$	$20.03^{+4.58}_{-4.89}$	$21.41^{+1.78}_{-2.19}$	$0.65^{+0.23}_{-0.3}$	$-0.04^{+0.21}_{-0.17}$	$0.36^{+0.27}_{-0.42}$	12	0.18	0.09	$<10^{-2}$	$<10^{-2}$
GW170608	$10.97^{+1.72}_{-5.45}$	$7.6^{+2.19}_{-1.36}$	$7.94^{+0.18}_{-0.19}$	$0.69^{+0.36}_{-0.28}$	$0.03^{+0.07}_{-0.19}$	$0.36^{+0.27}_{-0.45}$	1.41	13	10	$<10^{-2}$	$<10^{-2}$
GW170729	$50.27^{+10.24}_{-16.21}$	$33.97^{+10.07}_{-9.08}$	$35.45^{+4.78}_{-6.48}$	$0.68^{+0.28}_{-0.28}$	$0.37^{+0.25}_{-0.21}$	$0.44^{+0.28}_{-0.35}$	1.01	2.28	1.04	90	59
GW170809	$34.98^{+5.86}_{-8.27}$	$23.84^{+5.17}_{-5.14}$	$24.91^{+1.66}_{-2.12}$	$0.68^{+0.24}_{-0.28}$	$0.08^{+0.17}_{-0.17}$	$0.35^{+0.26}_{-0.43}$	5.81	2.85	0.51	$<10^{-2}$	$<10^{-2}$
GW170814	$30.6^{+2.96}_{-5.58}$	$25.22^{+4.04}_{-2.81}$	$24.1^{+1.13}_{-1.39}$	$0.83^{+0.23}_{-0.15}$	$0.07^{+0.12}_{-0.12}$	$0.48^{+0.36}_{-0.41}$	3.58	6.94	0.88	$<10^{-2}$	$<10^{-2}$
GW170818	$35.37^{+4.72}_{-7.45}$	$26.73^{+5.23}_{-4.28}$	$26.56^{+1.72}_{-2.11}$	$0.76^{+0.25}_{-0.21}$	$-0.09^{+0.21}_{-0.18}$	$0.49^{+0.34}_{-0.37}$	3.58	4.32	1.73	$<10^{-2}$	$<10^{-2}$
GW170823	$39.53^{+6.69}_{-11.2}$	$29.04^{+7.83}_{-6.74}$	$29.19^{+3.63}_{-4.62}$	$0.74^{+0.3}_{-0.23}$	$0.09^{+0.26}_{-0.22}$	$0.42^{+0.31}_{-0.41}$	0.0	4.32	1.73	$<10^{-2}$	$<10^{-2}$

Note. Columns (2)–(7) show the median and 90% symmetric credible intervals on selected source parameters (Abbott et al. 2021a). Columns (8)–(11) report our estimated Bayes factors for our fiducial AGN versus GWTC-2 models.

(This table is available in machine-readable form.)

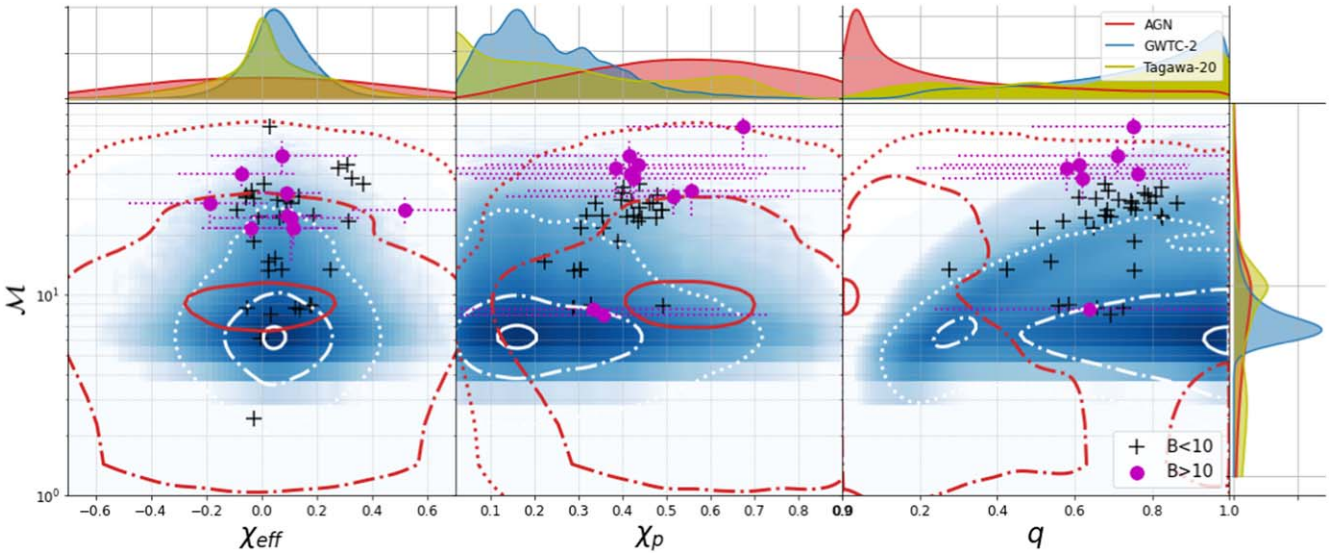

Figure 1. Probability densities for the GWTC-2 model and reconstructed parameters for gravitational-wave events. The distributions and reconstructed values are shown for $\mathcal{M} - \chi_{\rm eff}$ (left), $\mathcal{M} - \chi_{\rm p}$ (middle), and $\mathcal{M} - q$ (right). Probability densities for single parameters marginalized over other parameters are also shown on the top and on the right for the GWTC-2 model, for the fiducial AGN model in this work, and for the AGN model of Tagawa et al. (2021a) (see the legend). Gravitational-wave events with Bayes factor $\mathcal{B} > 10$ ($\mathcal{B} < 10$) are shown in magenta (black). For the $\mathcal{B} > 10$ case we also show the 90% credible intervals of the reconstructed parameters (dotted lines). For the GWTC-2 model probability density, white lines mark the 95%, 65%, and 10% credible areas. The red lines mark the 95%, 65%, and 10% credible areas for the fiducial AGN model in this work. Note that the shown probability densities depict the expected rate of occurrence, i.e., they are not weighted by the expected detection volume, while the distributions of the parameters of observed events are affected by their detection volumes.

Virgo's O1–O3a detected sample, which is comparable to the number of events we identified with $\mathcal{B} > 10$.

Figure 2 shows the expected number of detections per unit mass as a function of $\mathcal{M}$ and m_1 for both AGN and GWTC-2 models. For our fiducial AGN model, this spectrum was normalized so it corresponds to a total of four detections for $\mathcal{M} > 40\ M_\odot$, corresponding to 15 detections for all masses. For the GWTC-2 model the curve corresponds to a total of 47 detections, i.e., the number of LIGO–Virgo's detections during O1–O3a. We see that, below $50\,M_\odot$, the GWTC-2 spectrum is substantially above the spectrum of our suspected AGN detections. This changes above $\sim 50\,M_\odot$, where our fiducial AGN channel dominates, especially above the maximum mass $\sim 90\,M_\odot$ allowed by the GWTC-2 model.

The above results rely on the assumption that the GWTC-2 model accurately represents the underlying binary distribution.

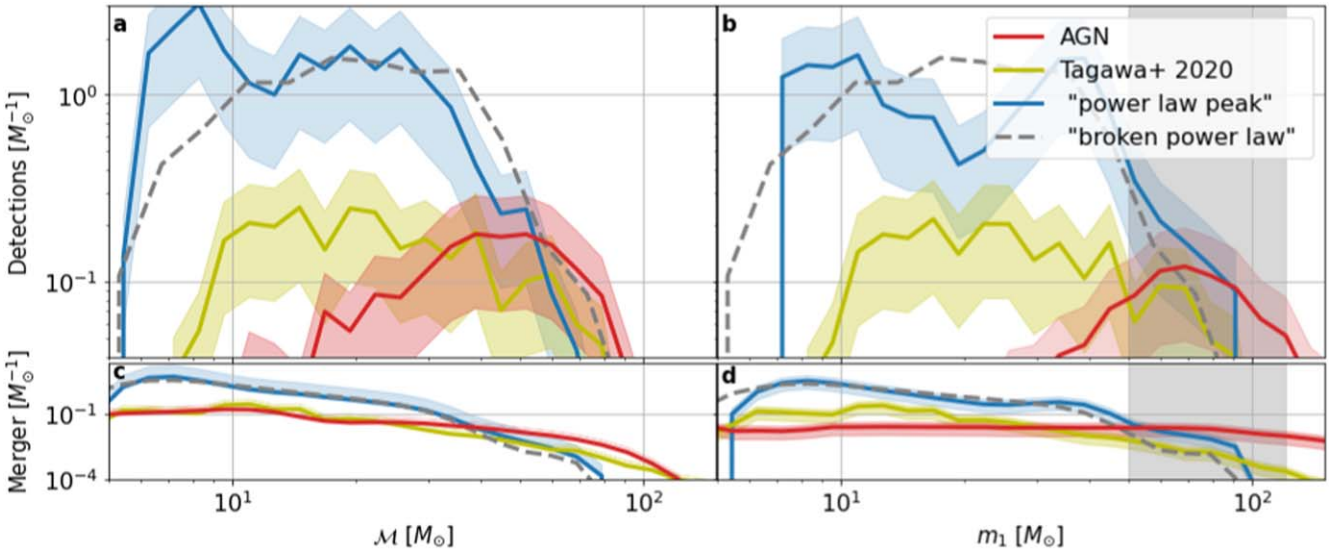

Figure 2. Detection and merger spectra of $\mathcal{M}$ and m_1 for the AGN and GWTC-2 models. Expected number of detections ((a) and (b)) and expected merger rate ((c) and (d)) per unit mass as functions of $\mathcal{M}$ ((a) and (c)) and m_1 ((b) and (d)) for the AGN model (red), Tagawa model+2021 (yellow), and the GWTC-2 model (blue; "power-law peak" model from Abbott et al. 2021b). For comparison, we also show the "broken power-law" model from Abbott et al. (2021b) (gray dashed). Vertical gray bands mark the expected range of the BH pair-instability mass gap ∼50–120 $M_\odot$.

This is not necessarily the case, which might bias our Bayes factors to favor high-mass events as the AGN channel mainly produces events there. In addition, the GWTC-2 model was fit on all events, including AGN-assisted mergers, although this makes the performed model comparison more conservative.

To understand our rate estimates in a more independent way of our model comparison, we can consider the following question: what is the maximum AGN-assisted merger rate that is consistent with the observed BH mass distribution and the overall LIGO–Virgo detection rate? For both of our AGN models, we found that this question gives a similar rate to what we found through model comparison, i.e., about $2.5\,\mathrm{Gpc^{-3}\,yr^{-1}}$. This can be seen in Figure 2: for both AGN models this rate gives a detected mass spectrum similar to that observed by LIGO–Virgo at high masses, while giving a lower-than-observed spectrum for lower masses. Further increasing the rate would, however, "overproduce" high-mass detections, making it inconsistent with observations.

6. Conclusions

We carried out a Bayesian model comparison to probe which of LIGO–Virgo's binary mergers detected within the O1, O2, and O3a observing periods could be of AGN origin and to estimate the rate of AGN-assisted mergers. We used the one fiducial model from GWTC-2 as a conservative comparison as it is fit to the observed data and therefore also includes events that are possibly of AGN origin. We used the obtained Bayes factors comparing our fiducial AGN model and the best-fit GWTC-2 model to examine the population of AGN-assisted mergers within the population detected by LIGO–Virgo. Our conclusions are summarized below:

1. Out of the 47 events in the GWTC-2 catalog, 12 have Bayes factor $\mathcal{B} > 10$, i.e., are better fit by our fiducial AGN-disk model than by the GWTC-2 distribution.
2. Using the highest-mass events, which are all better explained by our fiducial AGN model, we estimated the total BH merger rate in AGNs to be $2.5 \pm 0.7\,\mathrm{Gpc^{-3}\,yr^{-1}}$ (90% CL statistical uncertainty, not including any model uncertainty). This is 2%−30% of the total merger rate $23.9^{+14.9}_{-8.6}\ \mathrm{Gpc^{-3}\,yr^{-1}}$ estimated from all LIGO–Virgo detections. We find a similar rate estimate if we determine the maximum AGN contribution for our fiducial model that is consistent with LIGO–Virgo's detected mass spectrum.
3. The detected mass distribution expected from our fiducial AGN model reproduces well (without any fit parameters) the GWTC-2 distribution fit to observations at high masses ($\mathcal{M} \gtrsim 40\ M_\odot$ or $m_1 \gtrsim 50\ M_\odot$). Based on this model, AGNs only marginally contribute to the detected lower-mass mergers ($5\,M_\odot \lesssim m \lesssim 50\ M_\odot$); therefore, the mass spectrum of BHs in this mass range could be representative of non-AGN formation channels observed by LIGO–Virgo.

Several caveats remain regarding the above conclusions. First, our analysis relies on the fact that the GWTC-2 parametric model (Abbott et al. 2021b) reasonably covers the true distribution of detected mergers. While the model is well motivated by astrophysical expectations and observed features, we cannot quantitatively assess its accuracy here. An inaccurate model could mean that some of our Bayes factors are overestimated. Second, other merger channels, for example hierarchical mergers in non-AGN environments, could similarly result in a BH mass distribution that extends to high masses and accounts for some of the most massive events we associate here with AGNs. Third, many of the parameters in our AGN model are not well constrained observationally. This introduces an uncertainty in our results that is difficult to quantitatively assess. Results from the second AGN model (Tagawa et al. 2021a) considered here provide some qualitative idea of this uncertainty. With the model of Tagawa et al. (2021a) that produces mergers with low binary masses, we found no source with high-Bayes-factor preference for an AGN origin except GW190426_152155. (GW190426_152155 was not used when fitting the GWTC-2 model.) Fourth, here we did not take into account the fact that some AGN-assisted mergers could be highly eccentric (Samsing et al. 2020; Tagawa et al.

2021b), which would affect their detectability and the accuracy of their mass and spin reconstruction. These caveats merit further study. Similarly, other approaches also used to analyze the hierarchical component are discussed in Doctor et al. (2020), McKernan et al. (2020), and Abbott et al. (2021b). Fifth, in the above results the Bayes factor was used for model comparison, which does not take into account prior probabilities of our AGN and null models. Considering our results as reasonably accurate, however, the two prior probabilities are only a factor of 3 different; therefore, events favored by a Bayes factor of >10 are still favored by an odds ratio of >3.

Nonetheless, assuming that the above described AGN contribution is accurate, we can make predictions on some expected features of mergers and future detections:

1. Future observations should uncover mergers with BH masses $>100\ M_{\odot}$, which could represent up to a few percent of detected events. Many such massive events should have high precessing spins.
2. The large fractional contribution of AGNs enhances the utility of correlating the localization of the detected mergers with catalogs of AGNs. A 30% contribution may be identifiable from several hundred detections (all channels included), assuming sufficiently complete AGN catalogs (Bartos et al. 2017a).

We gratefully acknowledge the support of LIGO and Virgo for provision of computational resources. I.B. acknowledges the support of the National Science Foundation under grant #1911796 and of the Alfred P. Sloan Foundation. Z.H. was supported by NASA grant NNX15AB19G and NSF grants AST-2006176 and AST-1715661. This research has made use of data, software, and/or web tools obtained from the Gravitational Wave Open Science Center, a service of LIGO Laboratory, the LIGO Scientific Collaboration, and the Virgo Collaboration. LIGO is funded by the U.S. National Science Foundation. Virgo is funded by the French Centre National de Recherche Scientifique (CNRS), the Italian Istituto Nazionale della Fisica Nucleare (INFN) and the Dutch Nikhef, with contributions by Polish and Hungarian institutes. H.T. acknowledges support by the Grants-in-Aid for Basic Research by the Ministry of Education, Science and Culture of Japan (HT:17H01102, 17H06360). This material is based upon work supported by NSF's LIGO Laboratory which is a major facility fully funded by the National Science Foundation.

ORCID iDs

V. Gayathri https://orcid.org/0000-0002-7167-9888
Z. Haiman https://orcid.org/0000-0003-3633-5403
I. Bartos https://orcid.org/0000-0001-5607-3637

References

Aasi, J., Abbott, B. P., Abbott, R., et al. 2015, CQGra, 32, 074001
Abbott, B. P., Abbott, R., Abbott, T. D., et al. 2019, PhRvX, 9, 031040
Abbott, R., Abbott, T. D., Abraham, S., et al. 2021a, PhRvX, 11, 021053
Abbott, R., Abbott, T. D., Abraham, S., et al. 2021b, ApJL, 913, L7
Abbott, R., Abbott, T. D., Abraham, S., et al. 2020, PhRvL, 125, 101102
Acernese, F., Agathos, M., Agatsuma, K., et al. 2015, CQGra, 32, 024001
Antoni, A., MacLeod, M., & Ramirez-Ruiz, E. 2019, ApJ, 884, 22
Antonini, F., Murray, N., & Mikkola, S. 2014, ApJ, 781, 45
Bardeen, J. M. 1970, Natur, 226, 64
Bartos, I., Haiman, Z., Marka, Z., et al. 2017a, NatCo, 8, 831
Bartos, I., Kocsis, B., Haiman, Z., & Márka, S. 2017b, ApJ, 835, 165
Belczynski, K., Kalogera, V., & Bulik, T. 2002, ApJ, 572, 407
Belczynski, K., Klencki, J., Fields, C. E., et al. 2020, A&A, 636, A104
Binney, J., & Tremaine, S. 2008, Galactic Dynamics: Second Edition (Princeton, NJ: Princeton Univ. Press)
Carr, B. J., & Hawking, S. W. 1974, MNRAS, 168, 399
de Mink, S. E., & Mandel, I. 2016, MNRAS, 460, 3545
Di Carlo, U. N., Mapelli, M., Bouffanais, Y., et al. 2020, MNRAS, 497, 1043
Doctor, Z., Wysocki, D., O'Shaughnessy, R., Holz, D. E., & Farr, B. 2020, ApJ, 893, 35
Farmer, R., Renzo, M., de Mink, S., et al. 2020, ApJ, 902, L36
Gayathri, V., Bartos, I., Haiman, Z., et al. 2020, ApJL, 890, L20
Goldreich, P., Lithwick, Y., & Sari, R. 2002, Natur, 420, 643
Gondán, L., Kocsis, B., Raffai, P., & Frei, Z. 2018, ApJ, 860, 5
Hannam, M., Schmidt, P., Bohé, A., et al. 2014, PhRvL, 113, 151101
Kaaz, N., Schrøder, S. L., Andrews, J. J., Antoni, A., & Ramirez-Ruiz, E. 2021, arXiv:2103.12088
Kass, R. E., & Raftery, A. E. 1995, J. Am. Stat. Assoc., 90, 773
Kim, H., & Kim, W.-T. 2007, ApJ, 665, 432
Kim, H., Kim, W.-T., & Sánchez-Salcedo, F. J. 2008, ApJL, 679, L33
Kimpson, T. O., Spera, M., Mapelli, M., & Ziosi, B. M. 2016, MNRAS, 463, 2443
Szölgyén, Á., & Kocsis, B. 2018, PhRvL, 121, 101101
Li, Y.-P., Dempsey, A. M., Li, S., Li, H., & Li, J. 2021, ApJ, 911, 124
Lubow, S. H., Seibert, M., & Artymowicz, P. 1999, ApJ, 526, 1001
Mandel, I., Farr, W. M., & Gair, J. R. 2019, MNRAS, 486, 1086
Marchant, P., Langer, N., Podsiadlowski, P., Tauris, T. M., & Moriya, T. J. 2016, A&A, 588, A50
McKernan, B., Ford, K. E. S., Lyra, W., & Perets, H. B. 2012, MNRAS, 425, 460
McKernan, B., Ford, K. E. S., O'Shaughnessy, R., & Wysocki, D. 2020, MNRAS, 494, 1203
O'Leary, R. M., Kocsis, B., & Loeb, A. 2009, MNRAS, 395, 2127
Özel, F., & Freire, P. 2016, ARA&A, 54, 401
Portegies Zwart, S. F., & McMillan, S. L. W. 2000, ApJL, 528, L17
Portegies Zwart, S. F., & Yungelson, L. R. 1998, A&A, 332, 173
Samsing, J., Bartos, I., D'Orazio, D. J., et al. 2020, arXiv:2010.09765
Sigurdsson, S., & Hernquist, L. 1993, Natur, 364, 423
Stone, N. C., Metzger, B. D., & Haiman, Z. 2017, MNRAS, 464, 946
Tagawa, H., Haiman, Z., Bartos, I., & Kocsis, B. 2020a, ApJ, 899, 26
Tagawa, H., Haiman, Z., & Kocsis, B. 2020b, ApJ, 898, 25
Tagawa, H., Kocsis, B., Haiman, Z., et al. 2021a, ApJ, 908, 194
Tagawa, H., Kocsis, B., Haiman, Z., et al. 2021b, ApJL, 907, L20
Veske, D., Márka, Z., Sullivan, A. G., et al. 2020, MNRAS, 498, L46
Vitale, S., Gerosa, D., Farr, W. M., & Taylor, S. R. 2020, arXiv:2007.05579
Volonteri, M., Sikora, M., & Lasota, J.-P. 2007, ApJ, 667, 704
Woosley, S. E., & Heger, A. 2015, in Astrophysics and Space Science Library, Very Massive Stars in the Local Universe, 412, ed. J. S. Vink (Cham: Springer), 199
Yang, Y., Bartos, I., Haiman, Z., et al. 2019, ApJ, 876, 122
Yang, Y., Bartos, I., Haiman, Z., et al. 2020, ApJ, 896, 138
Yang, Y., Gayathri, V., Bartos, I., et al. 2020, ApJL, 901, L34